2010

A VERY METAL-POOR DAMPED LYMAN-α SYSTEM REVEALED THROUGH THE MOST ENERGETIC GRB 090926A

A. Rau

S. Savaglio

T. Kr¨ uhler

P. Afonso

J. Greiner

See next page for additional authors

The Astrophysical Journal, 720:862–871, 2010 September 1 doi:10.1088/0004-637X/720/1/862

A VERY METAL-POOR DAMPED LYMAN-α SYSTEM REVEALED THROUGH THE MOST ENERGETIC GRB 090926A

A. Rau[1], S. Savaglio[1], T. Krühler[1,2], P. Afonso[1], J. Greiner[1], S. Klose[3], P. Schady[1], S. McBreen[1,4], R. Filgas[1], F. Olivares E.[1], A. Rossi[3], and A. Updike[5]
[1] Max-Planck Institute for Extraterrestrial Physics, Giessenbachstrasse 1, Garching, 85748, Germany; arau@mpe.mpg.de
[2] Universe Cluster, Technische Universität München, Boltzmannstraße 2, 85748, Garching, Germany
[3] Thüringer Landessternwarte Tautenburg, Sternwarte 5, D-07778 Tautenburg, Germany
[4] School of Physics, University College Dublin, Dublin 4, Ireland
[5] Department of Physics and Astronomy, Clemson University, Clemson, SC 29634, USA
Received 2010 January 26; accepted 2010 July 13; published 2010 August 13

ABSTRACT

We present VLT/FORS2 spectroscopy and Gamma-ray Optical/Near-Infrared Detector optical/near-IR photometry of the afterglow of the bright *Fermi*/LAT GRB 090926A. The spectrum shows prominent Lyman-α absorption with $N_{\rm H\,I} = 10^{21.73\pm0.07}$ cm^{-2} and a multitude of metal lines at a common redshift of $z = 2.1062 \pm 0.0004$, which we associate with the redshift of the gamma-ray burst (GRB). The metallicity derived from S II is $\log(Z/Z_\odot) \approx -1.9$, one of the lowest values ever found in a GRB Damped Lyman-α (DLA) system. This confirms that the spread of metallicity in GRB-DLAs at $z \approx 2$ is at least two orders of magnitude. We argue that this spread in metallicity does not require a similar range in abundances of the GRB progenitors, since the neutral interstellar medium probed by the DLA is expected to be at a significant distance from the explosion site. The hydrogen column density derived from the *Swift*/XRT afterglow spectrum (assuming $\log(Z/Z_\odot) \approx -1.9$) is approx. $\approx$100 times higher than the $N_{\rm H\,I}$ obtained from the Lyman-α absorptions. This suggests either a large column density of ionized gas or a higher metallicity of the circum-burst medium compared to the gas traced by the DLA. We also discuss the afterglow light curve evolution and energetics. The absence of a clear jet-break like steeping until at least 21 days post-burst suggests a beaming-corrected energy release of $E_\gamma > 3.5 \times 10^{52}$ erg, indicating that GRB 090926A may have been one of the most energetic bursts ever detected.

Key words: gamma-ray burst: general – X-rays: individual (GRB 090926A)

Online-only material: color figures, machine-readable table

1. INTRODUCTION

For the brief moments of their existence, gamma-ray bursts (GRBs) and their X-ray/optical counterparts are the brightest beacons in the universe. The afterglow luminosities and simple power-law shaped spectra make them ideal background lights for probing the conditions in their host galaxies and in intervening systems through absorption line spectroscopy. Although the afterglows fade away within hours to days, rapid follow-up observations have been performed for a number of GRBs and have revealed tell-tale features of the circum-stellar medium around the progenitor and the interstellar medium (ISM; e.g., Castro et al. 2003). These studies provided otherwise hidden details of the kinematics (e.g., Klose et al. 2004; Fox et al. 2008), excitation (e.g., Vreeswijk et al. 2007), dust and gas content (e.g., Savaglio & Fall 2004; Prochaska et al. 2006), and the chemical abundances (e.g., Savaglio et al. 2003; Fynbo et al. 2006) in the star-forming, low-mass galaxies that host GRBs (e.g., Le Floc'h et al. 2003; Christensen et al. 2004; Rau et al. 2005; Savaglio et al. 2009).

In this paper, we present photometric and spectroscopic follow-up observations of the bright GRB 090926A, concentrating on the energetics of the burst and the chemical enrichment traced by the optical afterglow. GRB 090926A was discovered by the Gamma-ray Burst Monitor (GBM; Meegan et al. 2009) on board the *Fermi Gamma-ray Space Telescope* on 2009 September 26 at $T_0 = 04{:}20{:}27$ UT and belongs to the long-duration class ($T_{90} = 20 \pm 2$ s, Bissaldi 2009). Further detections of the prompt emission were reported from *Fermi*/LAT (Uehara et al. 2009; Bissaldi et al. 2009), *Suzaku*-WAM (Noda et al. 2009), and *Konus-Wind* (Golenetskii et al. 2009), and the X-ray (*Swift*/XRT, Vetere et al. 2009) and optical (*Swift*/UVOT, Gronwall & Vetere 2009; Skynet, Haislip et al. 2009a) afterglows were also detected. A redshift of $z = 2.1062$ was measured with VLT/X-Shooter observations (Malesani et al. 2009).

Throughout the paper, we adopt concordance ΛCDM cosmology ($\Omega_{\rm M} = 0.27$, $\Omega_\Lambda = 0.73$, $\rm H_0 = 71$ (km s^{-1}) Mpc^{-1}), and the convention that the flux density of the GRB afterglow can be described as $F_\nu \propto \nu^{-\beta} t^{-\alpha}$.

2. OBSERVATIONS AND DATA ANALYSIS

2.1. Photometry

Our follow-up photometry was initiated on 2009 September 27.03 UT (73 ks post-trigger) once the X-ray afterglow had been localized and its position became accessible with the seven-band Gamma-ray Optical/Near-Infrared Detector (GROND; Greiner et al. 2008) on the MPI/ESO 2.2 m telescope at La Silla, Chile. Observations continued until 28 days post-burst (see Table 1 and Table 2). Due to technical problems with the near-IR channels, observations in J and H started only in the third night, and K_S-band imaging is available only from the fourth night on. The afterglow was detected in all seven bands ($g'r'i'z'JHK_S$), as expected from the spectroscopic redshift. The best localization was measured to be $\alpha_{J2000} = 23{:}33{:}36.04$, $\delta_{J2000} = -66{:}19{:}26.6$ with a systematic uncertainty of $0\farcs2$ compared to USNO-B1 (Monet et al. 2003), consistent with

Table 1
Log of GROND Optical Photometry

$T_{\rm mid} - T_0$ (ks)	Exposure (s)	Brightness[a] $\rm mag_{AB}$[b]			
		g'	r'	i'	z'
73.16	115	19.00 ± 0.03	18.70 ± 0.02	18.54 ± 0.03	18.33 ± 0.03
73.34	115	18.98 ± 0.02	18.70 ± 0.02	18.53 ± 0.02	18.35 ± 0.03
73.52	115	18.98 ± 0.02	18.68 ± 0.02	18.55 ± 0.02	18.35 ± 0.03
73.44	115	18.96 ± 0.02	18.68 ± 0.02	18.51 ± 0.02	18.35 ± 0.03
73.91	115	18.93 ± 0.03	18.67 ± 0.02	18.53 ± 0.03	18.35 ± 0.03
74.10	115	18.95 ± 0.02	18.70 ± 0.02	18.51 ± 0.02	18.36 ± 0.03
74.30	115	18.95 ± 0.02	18.70 ± 0.02	18.52 ± 0.02	18.35 ± 0.03
74.49	115	18.95 ± 0.02	18.67 ± 0.02	18.50 ± 0.02	18.33 ± 0.02
74.81	375	18.94 ± 0.02	18.67 ± 0.02	18.49 ± 0.02	18.31 ± 0.03
75.26	375	18.92 ± 0.02	18.67 ± 0.02	18.48 ± 0.02	18.32 ± 0.02
75.71	375	18.89 ± 0.02	18.64 ± 0.02	18.46 ± 0.02	18.29 ± 0.02
76.16	375	18.90 ± 0.02	18.65 ± 0.02	18.48 ± 0.02	18.31 ± 0.02
76.77	115	18.89 ± 0.02	18.65 ± 0.02	18.45 ± 0.03	18.27 ± 0.03
76.77	115	18.87 ± 0.02	18.63 ± 0.02	18.47 ± 0.02	18.25 ± 0.03
76.87	115	18.88 ± 0.02	18.62 ± 0.02	18.45 ± 0.02	18.27 ± 0.03
77.06	115	18.91 ± 0.02	18.62 ± 0.02	18.48 ± 0.02	18.27 ± 0.03
83.19	115	18.74 ± 0.02	18.50 ± 0.02	18.36 ± 0.02	18.20 ± 0.03
83.37	115	18.75 ± 0.02	18.51 ± 0.02	18.33 ± 0.02	18.21 ± 0.02
83.56	115	18.77 ± 0.02	18.52 ± 0.02	18.36 ± 0.02	18.18 ± 0.02
83.75	115	18.78 ± 0.02	18.49 ± 0.02	18.36 ± 0.02	18.21 ± 0.02
83.95	115	18.74 ± 0.02	18.52 ± 0.02	18.37 ± 0.02	18.20 ± 0.03
84.14	115	18.74 ± 0.02	18.52 ± 0.02	18.35 ± 0.02	18.23 ± 0.02
84.33	115	18.75 ± 0.02	18.54 ± 0.02	18.37 ± 0.02	18.19 ± 0.02
84.53	115	18.74 ± 0.02	18.52 ± 0.02	18.40 ± 0.02	18.18 ± 0.02
84.73	115	18.74 ± 0.02	18.53 ± 0.02	18.40 ± 0.02	18.22 ± 0.03
84.92	115	18.78 ± 0.02	18.52 ± 0.02	18.38 ± 0.02	18.22 ± 0.02
85.11	115	18.76 ± 0.02	18.54 ± 0.02	18.39 ± 0.02	18.22 ± 0.02
85.31	115	18.76 ± 0.02	18.52 ± 0.02	18.38 ± 0.02	18.21 ± 0.02
91.58	115	18.89 ± 0.02	18.68 ± 0.02	18.49 ± 0.02	18.37 ± 0.03
91.76	115	18.92 ± 0.02	18.67 ± 0.02	18.52 ± 0.02	18.37 ± 0.02
91.95	115	18.87 ± 0.02	18.69 ± 0.02	18.53 ± 0.02	18.40 ± 0.03
92.15	115	18.89 ± 0.02	18.69 ± 0.02	18.51 ± 0.02	18.33 ± 0.03
92.35	115	18.89 ± 0.03	18.68 ± 0.02	18.50 ± 0.03	18.36 ± 0.03
92.54	115	18.91 ± 0.02	18.69 ± 0.02	18.54 ± 0.02	18.37 ± 0.03
92.74	115	18.92 ± 0.02	18.69 ± 0.02	18.54 ± 0.02	18.36 ± 0.03
92.93	115	18.94 ± 0.03	18.69 ± 0.02	18.52 ± 0.03	18.36 ± 0.03
93.14	115	18.97 ± 0.03	18.74 ± 0.03	18.53 ± 0.04	18.36 ± 0.04
93.33	115	18.99 ± 0.02	18.72 ± 0.03	18.55 ± 0.03	18.38 ± 0.03
93.51	115	18.90 ± 0.02	18.73 ± 0.03	18.53 ± 0.03	18.38 ± 0.04
93.71	115	18.94 ± 0.03	18.72 ± 0.02	18.53 ± 0.03	18.40 ± 0.03
102.15	115	19.03 ± 0.03	18.85 ± 0.03	18.63 ± 0.04	18.45 ± 0.06
102.33	115	19.08 ± 0.02	18.80 ± 0.02	18.65 ± 0.03	18.49 ± 0.04
102.52	115	19.06 ± 0.02	18.83 ± 0.02	18.65 ± 0.03	18.54 ± 0.05
102.72	115	19.04 ± 0.02	18.80 ± 0.02	18.65 ± 0.02	18.48 ± 0.03
102.92	115	19.05 ± 0.02	18.84 ± 0.02	18.65 ± 0.03	18.47 ± 0.04
103.11	115	19.08 ± 0.02	18.81 ± 0.02	18.69 ± 0.03	18.46 ± 0.04
103.31	115	19.09 ± 0.02	18.87 ± 0.02	18.68 ± 0.02	18.46 ± 0.03
103.50	115	19.07 ± 0.02	18.84 ± 0.02	18.69 ± 0.02	18.47 ± 0.03
103.71	115	19.12 ± 0.02	18.86 ± 0.02	18.69 ± 0.03	18.53 ± 0.04
103.90	115	19.13 ± 0.02	18.85 ± 0.02	18.68 ± 0.03	18.51 ± 0.04
104.09	115	19.09 ± 0.02	18.84 ± 0.02	18.69 ± 0.02	18.53 ± 0.03
104.29	115	19.09 ± 0.02	18.83 ± 0.02	18.71 ± 0.02	18.50 ± 0.03
166.36	115	19.88 ± 0.06	19.72 ± 0.04	19.50 ± 0.06	19.43 ± 0.06
166.55	115	19.90 ± 0.05	19.66 ± 0.04	19.57 ± 0.05	19.39 ± 0.07
166.74	115	19.92 ± 0.05	19.69 ± 0.03	19.55 ± 0.04	19.40 ± 0.06
166.94	115	19.93 ± 0.04	19.66 ± 0.03	19.53 ± 0.04	19.41 ± 0.05
167.13	115	19.88 ± 0.06	19.76 ± 0.05	19.52 ± 0.06	19.36 ± 0.04
167.32	115	19.94 ± 0.07	19.70 ± 0.04	19.55 ± 0.05	19.37 ± 0.07
167.51	115	19.90 ± 0.05	19.73 ± 0.03	19.60 ± 0.03	19.37 ± 0.04
167.70	115	19.89 ± 0.04	19.72 ± 0.03	19.50 ± 0.05	19.40 ± 0.05
173.77	115	20.13 ± 0.05	19.85 ± 0.03	19.62 ± 0.04	19.42 ± 0.06
173.95	115	20.06 ± 0.03	19.78 ± 0.02	19.68 ± 0.04	19.44 ± 0.04
174.15	115	20.08 ± 0.03	19.80 ± 0.03	19.62 ± 0.03	19.41 ± 0.03
174.35	115	20.11 ± 0.04	19.80 ± 0.03	19.60 ± 0.05	19.47 ± 0.05

Table 1
(Continued)

$T_{\rm mid} - T_0$ (ks)	Exposure (s)	Brightness[a] mag$_{\rm AB}$[b]			
		g'	r'	i'	z'
174.55	115	20.09 ± 0.05	19.81 ± 0.04	19.64 ± 0.04	19.44 ± 0.06
174.73	115	20.07 ± 0.03	19.82 ± 0.03	19.65 ± 0.03	19.41 ± 0.05
174.92	115	20.12 ± 0.04	19.82 ± 0.03	19.63 ± 0.03	19.44 ± 0.04
175.11	115	20.14 ± 0.03	19.78 ± 0.02	19.61 ± 0.03	19.47 ± 0.04
264.66	369	20.42 ± 0.05	20.15 ± 0.03	20.02 ± 0.04	19.79 ± 0.05
265.10	369	20.43 ± 0.04	20.17 ± 0.03	20.04 ± 0.03	19.77 ± 0.03
265.55	369	20.45 ± 0.04	20.19 ± 0.02	19.98 ± 0.03	19.79 ± 0.04
266.00	369	20.48 ± 0.04	20.21 ± 0.03	19.96 ± 0.03	19.71 ± 0.03
331.28	369	20.88 ± 0.08	20.57 ± 0.05	20.35 ± 0.05	20.15 ± 0.07
331.74	369	20.85 ± 0.05	20.57 ± 0.03	20.28 ± 0.03	20.09 ± 0.04
332.19	369	20.87 ± 0.05	20.55 ± 0.03	20.38 ± 0.04	20.17 ± 0.04
332.64	369	20.91 ± 0.04	20.59 ± 0.03	20.34 ± 0.04	20.14 ± 0.04
355.58	369	21.05 ± 0.06	20.80 ± 0.05	20.54 ± 0.05	20.34 ± 0.06
356.02	369	21.11 ± 0.05	20.83 ± 0.04	20.58 ± 0.05	20.29 ± 0.05
356.47	369	21.14 ± 0.04	20.75 ± 0.03	20.56 ± 0.04	20.30 ± 0.05
356.93	369	21.09 ± 0.06	20.84 ± 0.03	20.56 ± 0.04	20.40 ± 0.07
419.04	4 × 369	21.15 ± 0.10	20.88 ± 0.06	20.61 ± 0.07	20.45 ± 0.08
1300.22	4 × 369	23.45 ± 0.12	23.16 ± 0.09	>22.67	>22.47
1635.15	4 × 369	>23.48	23.64 ± 0.12	>22.68	>22.43
1808.91	8 × 369	24.13 ± 0.15	23.87 ± 0.12	>23.17	>22.98
2070.84	8 × 369	>24.24	24.02 ± 0.10	>23.44	>23.32
2840.06	12 × 369	>23.99	>23.98	>23.29	>23.02

Notes.
[a] Corrected for Galactic foreground reddening.
[b] For the SED fitting, the additional error of the absolute calibration of 0.05 mag was added.
(This table is also available in a machine-readable form in the online journal.)

Table 2
Log of GROND Near-IR Photometry

$T_{\rm mid} - T_0$ (ks)	Exposure [s] (s)	Brightness[a] mag$_{\rm AB}$[b]		
		J	H	K_S
265.36	120 × 10	19.44 ± 0.04	19.24 ± 0.04	...
331.98	120 × 10	19.88 ± 0.04	19.52 ± 0.04	19.27 ± 0.09
356.28	120 × 10	20.03 ± 0.04	19.77 ± 0.07	19.55 ± 0.09
419.06	120 × 10	20.01 ± 0.06	19.80 ± 0.07	19.57 ± 0.13

Notes.
[a] Corrected for Galactic foreground reddening and converted to AB magnitudes.
[b] For the SED fitting, the additional error of the absolute calibration of 0.05 (J and H) and 0.07 (K_S) mag was added quadratically.

the Skynet (Haislip et al. 2009b) and *Swift*/UVOT (Oates & Vetere 2009) afterglow positions.

The GROND data were reduced and analyzed with the standard tools and methods described in Krühler et al. (2008). The afterglow photometry was obtained using point-spread function fitting and calibrated against observations of the standard star field SA115-420 ($g'r'i'z'$) or against selected 2MASS stars (Skrutskie et al. 2006) (JHK_S). This resulted in 1σ accuracies of 0.04 mag ($g'z'$), 0.03 mag ($r'i'$), 0.05 mag (JH), and 0.07 mag (K_S). All magnitudes are corrected for Galactic foreground reddening of $E_{B-V} = 0.03$ mag (Schlegel et al. 1998).

2.2. Spectroscopy

Optical spectroscopy of the afterglow started on 2009 September 27.08 UT (78 ks post-burst) using the FOcal Reducer and low dispersion Spectrograph 2 (FORS2; Appenzeller et al. 1998) mounted on the 8.2 m ESO-VLT UT1 telescope in Paranal, Chile (Program ID: 083.D-0903). We obtained 2 × 1800 s integrations using the 600B grism (3600 Å– 6300 Å coverage) and a long slit of 1.″0 width. The average seeing was ≈0.″75 resulting in an effective spectral resolution of ≈4.5 Å FWHM at 4500 Å, or ≈300 km s^{-1}.

The data were reduced with standard IRAF (Tody 1993) routines, and spectra were extracted using an optimal (variance-weighted) method. Wavelength calibration was achieved using HeHgCd arc lamp exposures where a fit of 13 arc lines left 0.3 Å rms residuals. Spectro-photometric flux calibration was carried out against observations of the standard star Hz2 (Oke, unpublished[6]) taken on 2009 September 21.39 UT.[7] Corrections for slit losses due to finite slit width and for Galactic foreground extinction were applied.

3. RESULTS

3.1. Afterglow Spectral Energy Distribution and Light Curve

The optical/near-IR to X-ray spectral energy distributions (SEDs) compiled at approx. T_0 + 84 ks, +290 ks and +1.3 Ms, and the afterglow light curve are shown in Figures 1 and 2, respectively. Here, the *Swift*/XRT data had been extracted using the standard *xrtpipeline* task. The three SEDs are best described by simple power laws with $\beta_{ox} \approx 1.03$ and a rest-frame equivalent hydrogen column densities[8] of $N_{\rm H}$ =

[6] http://www.eso.org/sci/observing/tools/standards/spectra/hz2.html
[7] No suitable spectro-photometric standard star calibration frames have been obtained closer to the time of the afterglow observation.
[8] Assuming solar metallicity.

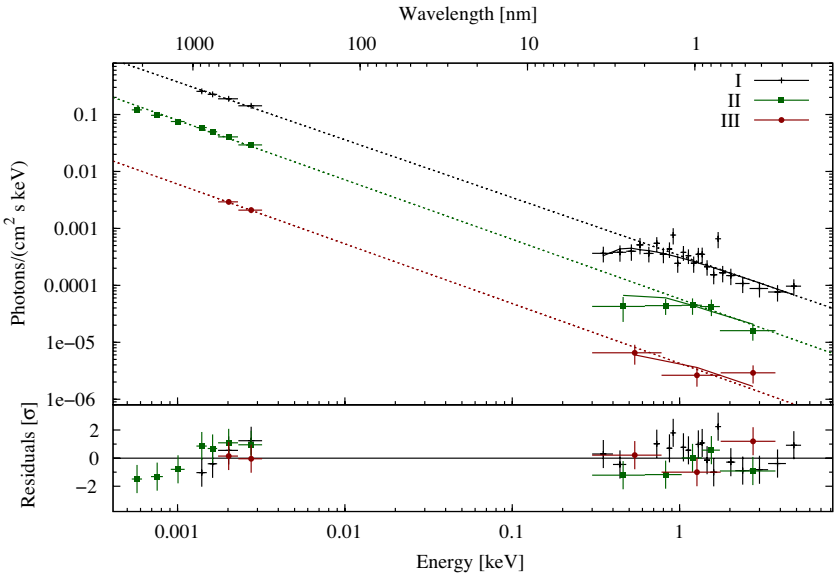

Figure 1. Combined GROND and *Swift*/XRT SED of the afterglow at $\approx T_0 + 84$ ks (interval I in Figure 2), $\approx T_0 + 290$ ks (II), and $\approx T_0 + 1.3$ Ms (III). Single power laws, modified by $N_H = 3.9^{+0.46}_{-0.36} \times 10^{21}$ cm^{-2} at the redshift of the burst in addition to the Galactic foreground extinction of 2.8×10^{20} cm^{-2} (Kalberla et al. 2005), fit best. The resulting slopes are $1.02^{+0.03}_{-0.02}$ (I, 90% uncertainty, $\chi^2 = 21.3$ / 24 d.o.f.), $1.05^{+0.04}_{-0.02}$ (II, 7.0/10), and $1.04^{+0.08}_{-0.06}$ (III, 2.6/3). Residuals to the fits are shown in the bottom panel.

(A color version of this figure is available in the online journal.)

$3.9^{+4.6}_{-3.6} \times 10^{21}$ cm^{-2} assuming the abundances of Wilms et al. (2000). The spectral slope derived from a power-law fit to the optical/near-IR data alone ($0.98^{+0.06}_{-0.07}$, $\chi^2 = 1.8$ for 5 d.o.f.) is consistent with the fit including the X-ray data, indicating very little intrinsic dust reddening. For the Small Magellanic Cloud-like dust attenuation law (Bouchet et al. 1985), we find a constraint of $A_V^{\rm host} < 0.1$ mag at 90% confidence. The absence of the characteristic 2175 Å bump (would be in the r' band) similarly restricts a Large Magellanic Cloud or Milky Way-like dust.

For the light curve analysis, we simultaneously fit the 0.3-10 keV data obtained from the *Swift*/XRT light curve repository (Evans et al. 2007) and the GROND optical/near-IR photometry, complemented by *Swift*/UVOT u-band measurements (Oates & Vetere 2009). Here, we used a model consisting of several smoothly connected broken power laws following the descriptions of Beuermann et al. (1999) and Liang et al. (2008). XRT observations started at $T_0 + 46.6$ ks (Vetere 2009) and revealed an initially decaying light curve with $\alpha_1 = 1.6 \pm 0.2$, consistent with the early UVOT photometry. This decay slope is at the boundary of the distributions of typically found pre- and post-jet-break slopes (Racusin et al. 2009). In the pre-jet scenario, α_1 would be roughly consistent with the closure relations ($\beta = 2\alpha/3$; Piran 2004) for the normal slow-cooling decay in a constant ISM with the cooling break frequency, ν_c (Sari et al. 1998), being above the XRT band. The corresponding electron index would be $p = 2\beta + 1 \approx 3$. In the post-jet-break case, the closure relations for a constant ISM and $\nu_c < \nu$ ($\beta = \alpha/2$) would be similarly well fulfilled. In this case, the electron index would lie closer to the canonical value, $p = 2\beta \approx 2$.

As reported by Haislip et al. (2009a), around T_0+(72.9 ± 0.7) ks the afterglow brightened again with a slope of $\alpha_2 = -2.7 \pm 0.3$ before peaking at $T_0 + (81.7 \pm 0.3)$ ks and then returning to the decay with $\alpha_3 = 1.63 \pm 0.01$. A second, similar, re-brightening episode likely occurred between $\approx T_0 + 180$ ks and $\approx T_0 + 250$ ks. However, only the subsequent decay with $\alpha_5 = 1.75 \pm 0.04$ is covered by our optical/near-IR data and the significant scatter in the X-ray light curve prevents a better constraint on this transition period. Deviations from simple power-law light curves are commonly observed in well-sampled afterglows and can be attributed to a variety of scenarios. The smooth rises and relatively constant (throughout the observed period) decay slopes suggest that the re-brightening in GRB 090926A could have been produced by multiple energy injection episodes, similar to the model of Björnsson et al. (2004) for GRB 021004 (de Ugarte Postigo et al. 2005). Alternative scenarios include processes intrinsic to the forward shock or related to discontinuities in the circumburst medium (e.g., Lazzati et al. 2002).

Our data suggest no jet-break-like steepening of the light curve before 21 days post-burst (3σ). However, we cannot rule out a jet break prior to the start of the afterglow observations at approx. $T_0 + 50$ ks ($T_0 + 16$ ks in the host frame). While possible, this would be comparably early. It appears more likely that XRT and GROND traced the normal spherical decay of the afterglow. Assuming the simplified model of a uniform jet plowing into a constant ISM environment[9] (Sari et al. 1999; Burrows & Racusin 2006), this implies a jet opening angle of $\theta > 9.^\circ 9$ and a beaming factor of $b \approx \theta^2/2 > 0.015$. The 10 keV–10 GeV fluence over T_{90} was $(2.47 \pm 0.03) \times 10^{-4}$ erg cm^{-2} (Bissaldi et al. 2009), corresponding to a total isotropic gamma-ray energy equivalent of $E_{\gamma,\rm iso} = (2.38 \pm 0.02) \times 10^{54}$ erg at 10 keV–10 MeV rest-frame energies. The equivalent jet-angle-corrected energy then amounts to $E_\gamma > 3.5 \times 10^{52}$ erg and would place GRB 090926A firmly among the most energetic bursts known (see also Cenko et al. 2010b), comparable to GRBs 060418 (Cenko et al. 2010a), 080916C (Greiner et al. 2009) and 090902B (McBreen et al. 2010).

[9] Assuming a number density of the ambient medium of 1 cm^{-3} and a radiative efficiency of 10%.

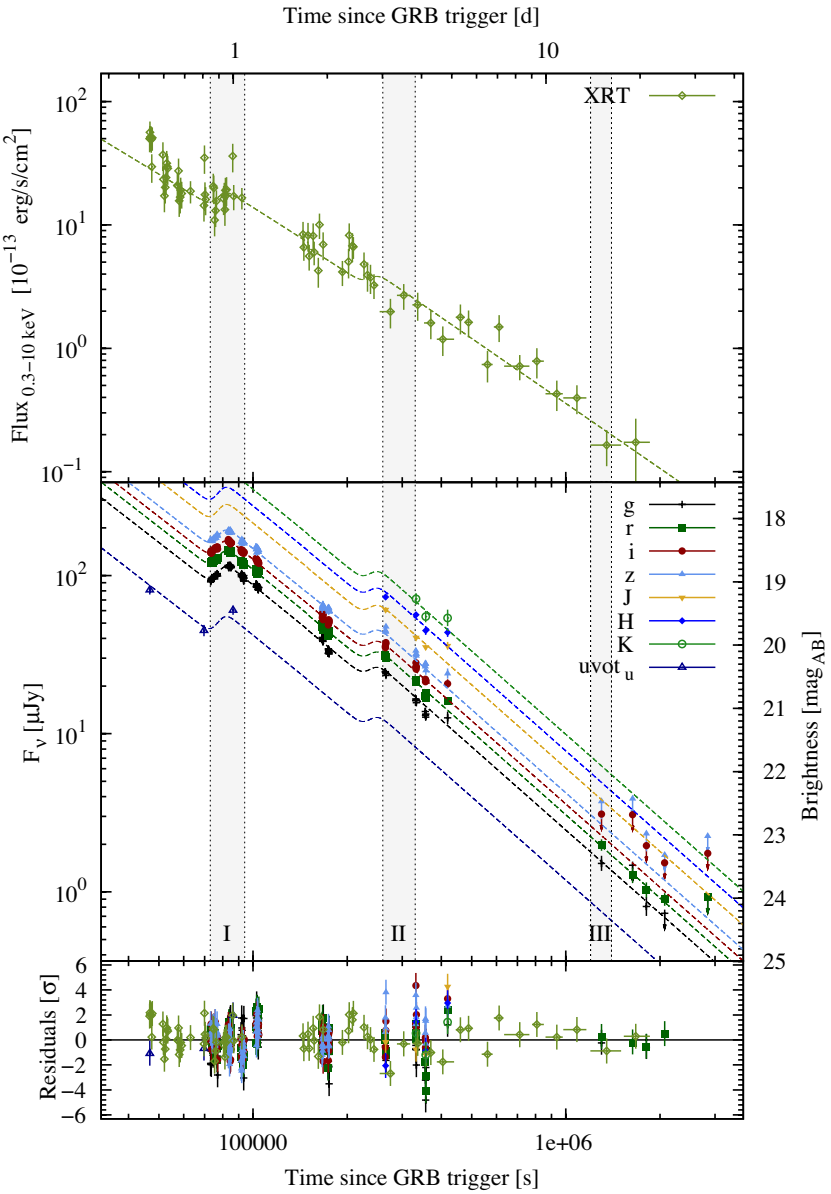

Figure 2. *Swift*/XRT (top panel) and GROND $g'r'i'z'$ JHK_S and *Swift*/UVOT u-band (middle) afterglow light curves. The dashed lines show a simplified model consisting of five smoothly connected power laws with slopes $\alpha_1 = 1.6 \pm 0.2$, $\alpha_2 = -2.7 \pm 0.3$, $\alpha_3 = 1.63 \pm 0.01$, and $\alpha_5 = 1.75 \pm 0.04$ and break times $T_1 = T_0 + (72.9 \pm 0.7)$ ks, $T_2 = T_0 + (81.7 \pm 0.3)$ ks, $T_3 \approx T_0 + 180$ ks, and $T_4 \approx T_0 + 250$ ks (α_4, the rising slope leading to the peak around T_4 is not constrained by our data). The smoothness parameters connecting the power-law segments were fixed to 10 (see also Beuermann et al. 1999). Time intervals for the SEDs in Figure 1 are shown as gray regions. Residuals are shown in the bottom panel. Data are not corrected for Galactic foreground extinction.

(A color version of this figure is available in the online journal.)

3.2. Afterglow Spectrum

The afterglow spectrum (Figure 3) displays a prominent Lyman-α absorption as well as numerous metal absorption lines at a common redshift of $z = 2.1062 \pm 0.0004$ (see Table 3 and Figure 4). Finally, two intervening absorption systems at $z = 1.748 \pm 0.001$ and $z = 1.946 \pm 0.001$ were localized based on the detection of C IV $\lambda\lambda$1548, 1550 doublets (see Table 4).

The column density of neutral hydrogen (H I) was obtained from the best-fit Voigt profile to the damping wings of the Lyman-α absorption feature (solid line in Figure 5) letting the redshift vary in the range measured from the metal lines. The dashed lines show the 1σ uncertainties for a fixed continuum fit. Systematic effects of the continuum placement may lead to sightly larger uncertainties. With $N_{\rm H\,I} = 10^{21.73 \pm 0.07}$ cm^{-2}, the resulting neutral hydrogen column density is similar to the median value observed in GRB afterglows (e.g., Savaglio 2006; Watson et al. 2007; Fynbo et al. 2009).

Column densities of metals were estimated using the curve of growth (COG) analysis (Spitzer 1978) and, if appropriate, the apparent optical depth (AOD) method (Savage & Sembach 1991). The COG analysis is routinely applied when high-resolution and high signal-to-noise spectroscopy is not available. It provides reliable results trough the linear approximation when the equivalent width of a line is EW< 0.1 Å and the effective Doppler parameter is $b > 20$ km s^{-1}. For stronger lines, the COG requires the detection of at least several lines with different oscillator strengths of the same ion. The AOD method is used for moderate to low EWs, provided that the effective Doppler parameter is not very low ($b \gtrsim 10$ km s^{-1}; Prochaska et al.

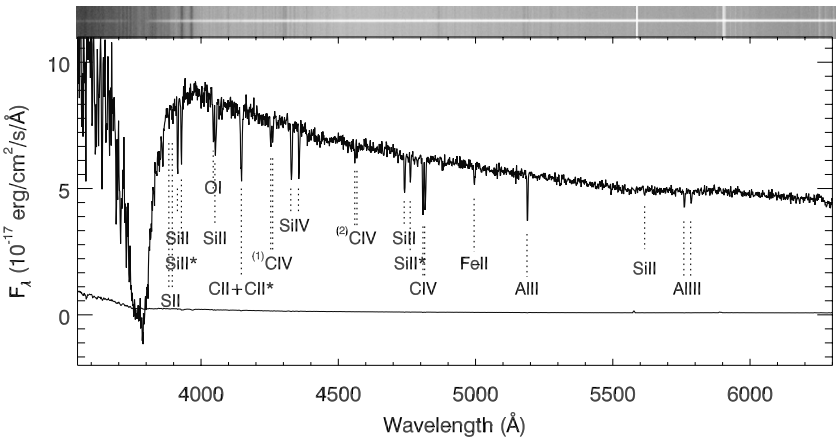

Figure 3. Observer frame VLT/FORS2 spectrum of the afterglow of GRB 090926A obtained 20 hr post-burst. The two-dimensional spectrum is shown at the top with telluric features remaining, while the fully reduced one-dimensional spectrum is presented in the bottom panel. Labels mark the most prominent absorption lines at a common redshift of $z = 2.1062 \pm 0.0004$, as well as C IV in two intermediate systems at (1) $z = 1.748 \pm 0.001$ and (2) $z = 1.946 \pm 0.001$. The background variance spectrum is shown by the bottom gray line.

Table 3
Line Properties of the $z = 2.1062 \pm 0.0004$ Absorption System

Ion	λ_{obs} (Å)	z	EW$_r$ (Å)	log N_X (cm^{-2})	b (km s^{-1})	[X/H]
H I	3775.9	...	...	21.73 ± 0.07	...	...
C II λ1334+C II*λ1335	4146.9	2.1064	0.720 ± 0.047[a]	...	...	...
Al II λ1670	5189.2	2.1059	0.461 ± 0.035	14.06 ± 0.24	...[b]	−2.12 ± 0.25
Al III λ1854	5760.9	2.1060	0.176 ± 0.032	13.25 ± 0.08	...[b]	...
Al III λ1862	5785.9	2.1060	0.143 ± 0.031	...	...	...
Si II λ1260	3914.8	2.1060	0.421 ± 0.037	14.97 ± 0.26	21.5 ± 2.4	−2.27 ± 0.27
Si II λ1304	4053.0	2.1073	<0.47[c]	...	...	...
Si II λ1526	4741.8	2.1058	<0.34[c]	...	...	...
Si II λ1808	5616.8	2.1062	0.066 ± 0.035	...[d]	...	...
Si II* λ1264	3928.5	2.1062	<0.39[c]	...	...	...
Si II* λ1309	4066.0	2.1055	0.074 ± 0.040	13.71 ± 0.13	...[b]	...
Si II* λ1533	4762.6	2.1059	0.172 ± 0.037	...	...	...
O I λ1302	4045.2	2.1064	0.315 ± 0.042	$15.40^{+0.37}_{-0.27}$	...[b]	$-3.02^{+0.38}_{-0.28}$
Fe II λ1608	4996.2	2.1062	0.194 ± 0.038	14.36 ± 0.14	...[b]	−2.86 ± 0.16
S II λ1250	3881.9	2.1055	0.070 ± 0.030	14.96 ± 0.15	...[b]	−1.89 ± 0.16
S II λ1254	3884.8	2.1064	0.093 ± 0.031	...	...	...
Ni II λ1317	...	...	<0.114[f]	...	...	...
Ni II λ1370	...	...	<0.219[c e]	...	...	...
Ni II λ1741	...	...	<0.110[e]	<14.1[f]	...[b]	< − 1.8
Zn II λ2026	...	...	<0.152[e]	<13.0[f]	...[b]	< − 1.2
C IV λ1548	4808.5	2.1059	0.511 ± 0.040	$15.85^{+0.01}_{-0.23}$	...[b]	...
C IV λ1550	4816.9	2.1061	0.491 ± 0.038	...	...	...
Si IV λ1393	4329.5	2.1064	0.507 ± 0.040	$14.13^{+0.20}_{-0.13}$	42^{+79}_{-30}	...
Si IV λ1402	4357.0	2.1059	0.366 ± 0.037	...	...	...
N V λ1238	...	...	>0.153	>13.8	...	...
N V λ1242	3860.9	2.1065	0.248 ± 0.030	$14.85^{+0.21}_{-0.16}$	...[b]	...

Notes.
[a] The two lines are blended.
[b] Effective Doppler parameter $b = 21.5$ km s^{-1} is fixed.
[c] The line is likely contaminated.
[d] The Apparent Optical Depth method from Savage & Sembach (1991) gives log$N = 15.03 \pm 0.25$ cm^{-2} for Si IIλ1808.
[e] 3σ upper limit.
[f] 3σ upper limit from EW upper limit.

2007). As an example, we applied the linear approximation of the COG and the AOD method to the weak Si II λ1808 line seen the spectrum of GRB 090926A. The resulting column density is consistent with the COG analysis of all transitions of Si II (see Table 3).

For the spectrum shown in Figure 3, the best estimate for the effective Doppler parameter comes from Si II ($b = 21.5 \pm 2.4$ km s^{-1}, Figure 6) which was also adopted for the analysis of other low ionization lines without constraints on b. The column densities derived using this b parameter are strictly correct only

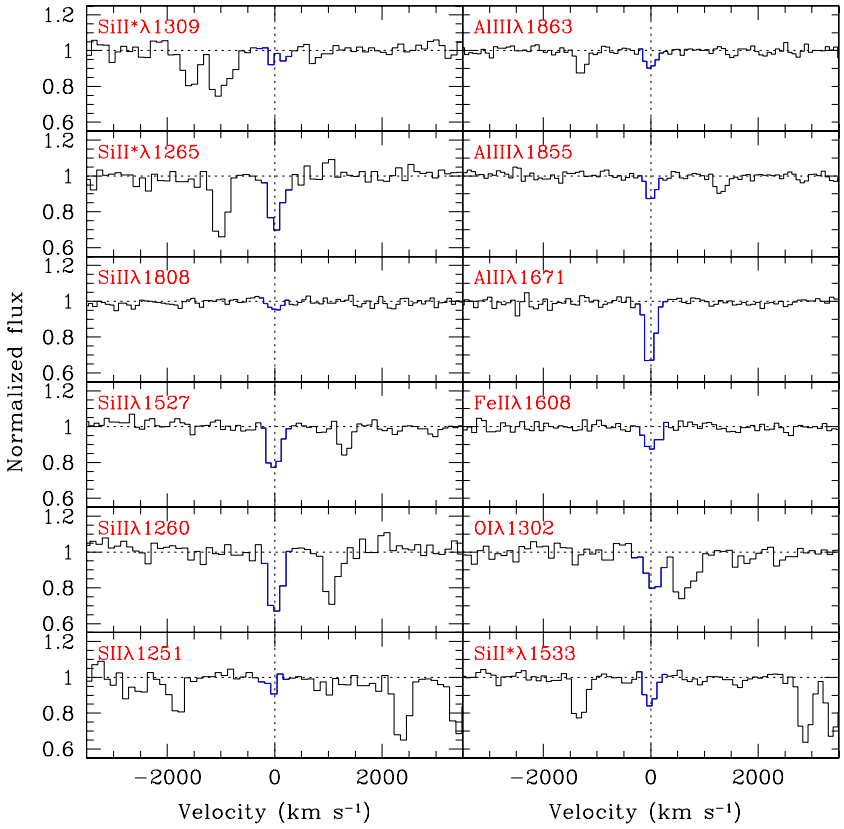

Figure 4. Velocity profiles for a selection of metal absorption lines. The vertical dotted lines correspond to zero velocity at a redshift of $z = 2.1062$.
(A color version of this figure is available in the online journal.)

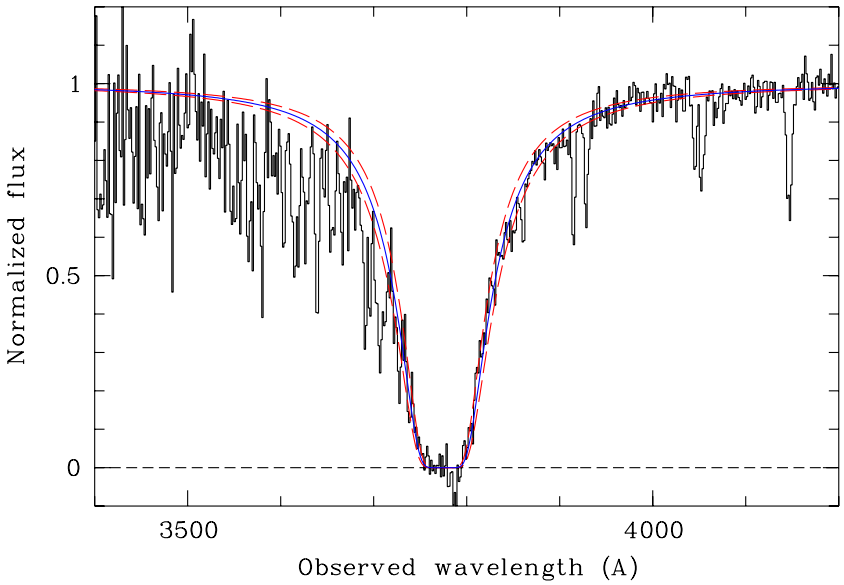

Figure 5. Lyman-α absorption at the redshift of the GRB host galaxy. The best fit of the damped profile with $N_{\rm H\,I} = 10^{21.73\pm0.07}$ cm^{-2} is shown as continuous line, while the dashed contours indicate the 1σ uncertainties (see the text).
(A color version of this figure is available in the online journal.)

for a single absorbing cloud. If the optical-depth distribution of absorbers is not smooth (e.g., bimodal), the resulting metal column densities can be underestimated (see Prochaska 2006, for a detailed discussion of this caveat). However, we note that the b value derived from Si II is small compared to previous measurements in GRB afterglow spectra (e.g., Savaglio & Fall 2004; Berger et al. 2006; Vreeswijk et al. 2006).

In a cloud with $N_{\rm H\,I} > 10^{20}$ cm^{-2}, the ionization level of the gas is low and the ionization correction can be neglected (Meiring et al. 2009). In this case, the abundance of an element X can be approximated by

$$[{\rm X/H}] = \log N_{\rm X\,II}/N_{\rm H\,I} - \log(N_{\rm X}/N_{\rm H})_{\odot}, \quad (1)$$

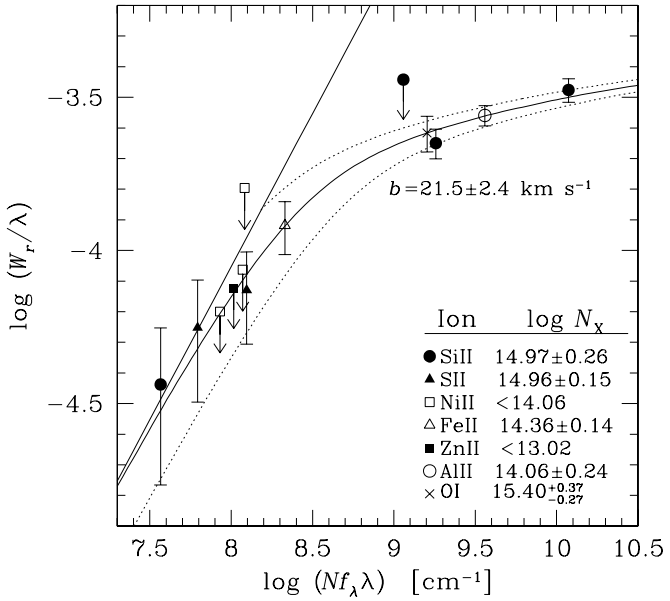

Figure 6. Curve of growth of low-ionization species in the DLA at $z = 2.1062$. The effective Doppler parameter $b = 21.5$ km s^{-1} has been obtained from the multiple absorption lines of Si II and adopted for all other ions.

where $N_{\rm X\,II}$ is the column density of singly ionized elements with ionization potential just above that of hydrogen.[10]

The abundances of Si, Fe, S, Al, and O were found between 0.1% and 1% of the solar value (see Table 3) with the average being $\log(Z/Z_\odot) \approx -2.5$. However, Fe, Al, and Si are potentially depleted. Oxygen suffers from the saturation region in the curve of growth and its column density is likely underestimated (e.g., Prochaska et al. 2003). As Zn is undetected, the least-depleted element remaining is S, which suggests a metallicity of $\log(Z/Z_\odot) \approx -1.9$ for the absorber. This is one of the lowest metallicities measured in a GRB Damped Lyman-α (DLA) spectrum.[11]

Another interesting finding, although with considerable uncertainty attached to it, is the apparent overabundance of silicon with respect to iron ($[{\rm Si/Fe}] = 0.59 \pm 0.30$), similar to a few previously observed GRB afterglows (e.g., Prochaska et al. 2007; de Ugarte Postigo et al. 2009). One explanation for the high [Si/Fe] ratio could be dust depletion of iron. The absence of significant dust extinction in the afterglow SED makes this scenario rather unlikely. Alternatively, this could indicate an α-enhancement arising from the different formation time scales of α-elements (short-lived massive stars) and Fe (type Ia supernovae). We note that this is in potential disagreement with the low oxygen content measured in the spectrum. However, as mentioned above, oxygen may be saturated and its column density thus underestimated.

The spectrum also shows a number of higher ionized lines (C IV, Si IV, and N V) which likely arise from regions distinct from those that produce the low-ionization transitions. Probable locations for the hot gas component are within the star-forming regions that hosted the GRB and/or in the halo of the host galaxy. In the case of Si, singly ionized and highly ionized species are detected in the spectrum. Here, the column density of the latter is low compared to that of the low-ionization transition.

4. DISCUSSION

4.1. Burst Energetics

GRB 090926A was likely one of the most energetic events in the sample of 16 bursts detected by both instruments onboard *Fermi*.[12] With a jet-angle-corrected energy release (for a uniform jet and a constant ISM) of $E_\gamma > 3.5 \times 10^{52}$ erg (but see caveats described in Section 3.1) GRB 090926A is rivaled only by GRB 080916C ($E_\gamma = (3.7 \pm 0.1) \times 10^{52}$ erg; Greiner et al. 2009) and by GRB 090902B ($E_\gamma > 2.2 \times 10^{52}$ erg; McBreen et al. 2010). This value of E_γ is close to the upper bound allowed from a maximally rotating neutron star in the magnetar model (Usov 1992) and would instead suggest the remnant of GRB 090926A to be a black hole.

We note that the inferred jet-angle-corrected energy release depends not only on whether the afterglow observations traced the pre-break or post-break slope but also on the assumption for the density distribution of the circumburst medium and for the jet geometry. A wind-shaped environment[13] would decrease the lower limit on the jet angle and thus relax the requirement on E_γ to $> 4.1 \times 10^{51}$ erg; (Livio & Waxman 2000; Greiner et al. 2003). However, the spectral and temporal slopes are in disagreement with the closure relations predicted for the wind model (Chevalier & Li 2000) and favor a constant ISM (Piran 2004). Alternatively, E_γ can be reduced by adopting a more realistic geometry than the top-hat (uniform) jet model (e.g., Rhoads 1997; Panaitescu & Mészáros 1999). A structured jet (Wijers et al. 1999) or a multi-component jet (e.g., Berger et al. 2003) would for instance allow the γ-ray emission to be tighter collimated than the long-wavelength counterpart. A similar discussion has been presented by Cenko et al. (2010a) for five energetic pre-*Fermi* bursts, indicating that in fact our understanding of the jet geometry in GRBs and their energetics are still incomplete. More insights into the jet structure require an increasing number of well-sampled, multi-wavelength afterglow light curves, such as routinely produced by *Swift* and GROND. Radio observations with the upcoming Expanded Very Large Array are expected to provide the first realistic constraint on E_γ for a larger sample of bursts.

4.2. Neutral Hydrogen Column Density

The $N_{\rm H\,I}$ derived from the Lyman-α absorption is similar to the equivalent $N_{\rm H}$ estimated from the soft X-ray absorption ($\log N_{\rm H} \sim 21.6$; see Section 3.1). The latter is dominated by α-chain elements and thus mainly a proxy for the oxygen column density assuming solar metallicity. If the oxygen abundance of the gas that causes the X-ray absorption was similar to that in the DLA (see Table 3), then the equivalent $N_{\rm H}$ would be approximately 2 orders of magnitude larger ($\log N_{\rm H} \sim 23.7$). While there is generally no correlation between X-ray and optical column densities for GRB afterglows (Watson et al. 2007), the ≈100 times larger equivalent $N_{\rm H}$ from the X-ray absorption compared to the Lyman-α profile fit for GRB 090926A would be one of the most extreme cases. It would require the large amount of hydrogen missed by the DLA to be ionized. The column density of $\log N_{\rm H} \approx 23.7$ would correspond

[10] In some cases, e.g., O and N, already the ionization potential of the neutral element, X I, is above that of hydrogen. Here, $[{\rm X/H}] = \log N_{\rm X\,I}/N_{\rm H\,I} - \log(N_{\rm X}/N_{\rm H})_\odot$ can be used.

[11] The current record holder is GRB 050730 at $z = 3.969$ with $\log(Z/Z_\odot) \approx -2.0$ (Chen et al. 2005; Starling et al. 2005).

[12] Status 2010, June 20.

[13] With a progenitor mass loss of 10^{-5} $M_\odot$ yr^{-1} and wind velocity of 1000 km s^{-1} (Chiosi & Maeder 1986).

Table 4
Intervening Absorption Systems

Ion	λ_{obs} (Å)	z	EW$_r$ (Å)
C IV λ1548	4254.1	1.7477	0.192 ± 0.039
C IV λ1550	4261.0	1.7478	0.175 ± 0.039
C IV λ1548	4560.7	1.9457	0.156 ± 0.041
C IV λ1550	4568.1	1.9458	0.067 ± 0.038

to a surface density of $\approx 4 \times 10^3\ M_\odot\ \mathrm{pc}^{-2}$, comparable to the H_2 surface densities of circumnuclear starbursts (Kennicutt 1998). Alternatively, the surface density can be reduced if the metallicity of the gas in the vicinity of the burst is higher than that traced by the DLA further out.

4.3. Metallicities in GRB Damped Lyman-α Systems

With $\log(Z/Z_\odot) \approx -1.9$ GRB 090926A has one of the most metal-poor DLA system found in a GRB so far. This is emphasized in Figure 7 where we show the metallicity as function of redshift for GRB 090926A together with 18 GRB-DLAs collected from the literature (Prochaska et al. 2007; Savaglio et al. 2009). The addition of GRB 090926A to the sample strengthens the observation that the metallicity spread in GRB-DLAs at redshifts 2–3 spans at least two orders of magnitude, from nearly solar (GRB 000926; Savaglio et al. 2003) to 1/100th solar (GRB 090926A and GRB 050922C; Prochaska et al. 2008). At higher redshifts, the sample becomes too small to draw statistically significant conclusions. However, no trend with redshift is visible. For the whole sample ($2.0 < z < 6.3$), the mean metallicity is $\langle \log(Z/Z_\odot) \rangle = -1.04 \pm 0.62$.

The immediate vicinity of a GRB is shaped by its progenitor and by the energetic explosion itself. UV photons produced during the GRB, or from massive stars in the star-forming region, ionize most of the circumburst medium out to a large distance (e.g., Perna & Loeb 1998; Waxman & Draine 2000). Empirical constraints on the ionization radius have been obtained from UV/optical absorption line measurements for a number of bursts and range from a few tens of parsec up to 1.7 kpc from the explosion site (e.g., Prochaska et al. 2006; Dessauges-Zavadsky et al. 2006; Vreeswijk et al. 2006). While these values are significantly larger than the ionization radii inferred from the N_H equivalent measurements in the X-rays and the GRB ultra-violet luminosity (≈3 pc; Watson et al. 2007), they indicate that the low-ionization lines in the UV/optical spectra are not assembled from the immediate vicinity of the burst but primarily from gas spread through kpc surrounding regions.

Metallicity dispersion within a galaxy is well studied in the local universe (e.g., Shaver et al. 1983; Cioni 2009) and similarly expected for the host galaxies of GRBs at higher redshift (e.g., Pontzen et al. 2009). This would suggest that the chemical abundance derived from a DLA may differ from that of the molecular cloud in which the GRB progenitor was formed. The extremely low metallicity revealed by the DLA of GRB 090926A does therefore not immediately require a similarly metal-poor progenitor star. It could have formed in a region with lower metallicity but may also have been more chemically enriched. As the same argument holds for the whole sample of GRB-DLAs depicted in Figure 7, the observed spread in metallicity may not directly represent a similar spread in the chemical composition of the GRB progenitors. Instead, the scatter likely arises from a combination of the internal gas-metallicity dispersion in the individual host galaxies as well as from the range of average metallicities of the galaxies included in the host sample.

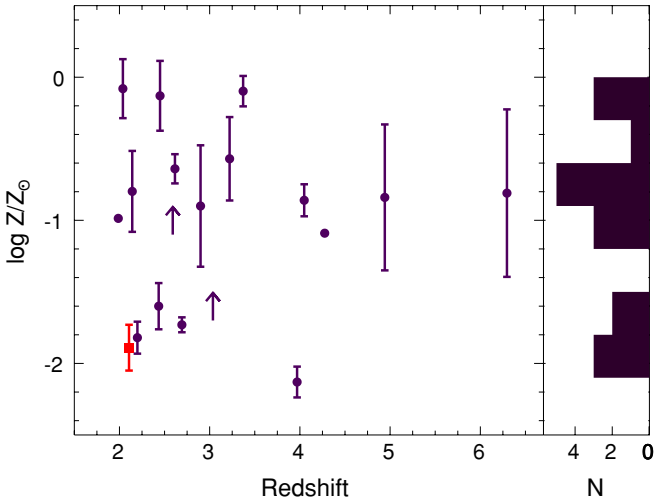

Figure 7. Left: metallicities found in GRB DLA systems as function of redshift. Filled circles mark metallicities selected from the literature with arrows indicating lower limits (adopted from Savaglio et al. 2009). The filled square shows the position of GRB 090926A. The two points without error bars are for GRBs 030226 and 050505 for which no uncertainties for $N_{H\,I}$ have been reported. Right: metallicity histogram in bins of $\Delta \log(Z/Z_\odot) = 0.3$. Lower limits have been excluded here.
(A color version of this figure is available in the online journal.)

Previous studies have demonstrated that GRBs are preferentially formed in the most luminous regions of their host galaxies, indicating high star formation activity (Fruchter et al. 2006; Svensson et al. 2010). Therefore, the lines of sight probed by their DLAs are not completely random paths through the host galaxies. Instead, they trace the neutral parts of the star-forming regions in which the progenitors were formed, as well as molecular clouds, interstellar medium, and halo material. These components will differ in their chemical compositions, and different sight lines will result in different net column densities and abundances. This interpretation has also been supported by hydrodynamical high-resolution simulations (Pontzen et al. 2009) which found metallicities of $10^{-2} < Z/Z_\odot < 1$ for different GRB-DLA sight lines through their host galaxies.

5. CONCLUSION

GRB 090926A was an event of two extremes. It was likely one of the most energetic explosions detected so far and simultaneously showed one of the most metal-poor GRB-DLA found until now. The large luminosity $E_\gamma > 3.5 \times 10^{52}$ erg, coupled with a bright slowly decaying afterglow, allowed a detailed study of the temporal evolution of the optical transient. It furthermore enabled high signal-to-noise spectroscopy of the afterglow as late as one day post-burst with VLT/FORS2.

With the spectrum, we confirmed the redshift of the host galaxy of $z = 2.1062 \pm 0.0004$ and discovered two intervening absorption systems at $z = 1.946 \pm 0.001$ and $z = 1.748 \pm 0.001$. Furthermore, we derived a neutral hydrogen column density of $N_{H\,I} = 10^{21.73 \pm 0.07}\ \mathrm{cm}^{-2}$ and a metallicity of the neutral ISM along the line of sight in the host galaxy of $\log(Z/Z_\odot) \approx -1.9$.

We close this paper with one reminder. The DLAs found in GRB afterglow spectra are predominantly probing the diverse

conditions and sub-structures within the host galaxies. They therefore allow important insight into the gas and metallicity distribution in galaxies at high redshift. The evolution of metallicity and column densities with redshift is, however, challenging to access with the current number of GRB-DLAs. A much larger sample of sight lines is required to first characterize the intrinsic gas-metallicity dispersions, and before GRB-DLAs can be used reliably for cosmic chemical evolution studies.

We thank the referee for the very helpful comments. The results are based on observations made with ESO Telescopes at the Paranal Observatories under program 083.D-0903. We are grateful to the ESO staff, in particular Stephane Brillant for the rapid execution of the observations. A. Rau also thanks Elena Mason for valuable discussion on the FORS2 data products. Part of the funding for GROND (both hardware as well as personnel) was generously granted from the Leibniz-Prize to Prof. G. Hasinger (DFG grant HA 1850/28-1). S.M.B. acknowledges support from a European Union Marie Curie European Reintegration grant within the 7th program under contract number PERG04-GA-2008-239176. T.K. acknowledges support by the DFG cluster of excellence Origin and Structure of the Universe. S.K. acknowledges support from DFG grant Kl 766/11-3.

REFERENCES

Appenzeller, I., et al. 1998, The Messenger, 94, 1
Berger, E., et al. 2003, Nature, 426, 154
Berger, E., et al. 2006, ApJ, 642, 979
Beuermann, K., et al. 1999, A&A, 352, L26
Bissaldi, E. 2009, GRB Coordinates Network, 9933, 1
Bissaldi, E., et al. 2009, GRB Coordinates Network, 9972, 1
Björnsson, G., Gudmundsson, E. H., & Jóhannesson, G. 2004, ApJ, 615, L77
Bouchet, P., et al. 1985, A&A, 149, 330
Burrows, D. N., & Racusin, J. 2006, Nuovo Cimento B, 121, 1273
Castro, S., et al. 2003, ApJ, 586, 128
Cenko, S. B., et al. 2010a, ApJ, 711, 641
Cenko, S. B., et al. 2010b, ApJ, submitted (arXiv:1004.2900)
Chen, H-W., Prochaska, J. X., Bloom, J. S., & Thompson, I. B. 2005, ApJ, 634, 25
Chevalier, R. A., & Li, Z. 2000, ApJ, 536, 195
Chiosi, C., & Maeder, A. 1986, ARA&A, 24, 329
Christensen, L., Hjorth, J., & Gorosabel, J. 2004, A&A, 425, 913
Cioni, M.-R. L. 2009, A&A, 506, 1137
de Ugarte Postigo, A., et al. 2005, A&A, 443, 841
de Ugarte Postigo, A., et al. 2010, A&A, 513, 42
Dessauges-Zavadsky, M., et al. 2006, ApJ, 648, L89
Evans, P. A., et al. 2007, A&A, 469, 379
Fox, A. J., et al. 2008, A&A, 491, 189
Fruchter, A. S., et al. 2006, Nature, 441, 463
Fynbo, J. P. U., et al. 2006, A&A, 451, L47
Fynbo, J. P. U., et al. 2009, ApJS, 185, 526
Golenetskii, S., et al. 2009, GRB Coordinates Network, 9959, 1
Greiner, J., et al. 2003, ApJ, 599, 1223
Greiner, J., et al. 2008, PASP, 120, 405
Greiner, J., et al. 2009, ApJ, 693, 1912
Gronwall, C., & Vetere, L. 2009, GRB Coordinates Network, 9938, 1
Haislip, J., et al. 2009a, GRB Coordinates Network, 9953, 1
Haislip, J., et al. 2009b, GRB Coordinates Network, 9937, 1
Kalberla, P. M. W., et al. 2005, A&A, 440, 775
Kennicutt, R.C. 1998, ApJ, 498, 541
Klose, S., et al. 2004, AJ, 128, 1942
Krühler, T., et al. 2008, ApJ, 685, 376
Lazzati, D., et al. 2002, A&A, 396, L5
Le Floc'h, E., et al. 2003, A&A, 400, 499
Liang, E., et al. 2008, ApJ, 675, 528
Livio, M., & Waxman, E. 2000, ApJ, 538, 187
Malesani, D., et al. 2009, GRB Coordinates Network, 9942, 1
McBreen, S., et al. 2010, A&A, 516, 71
Meegan, C., et al. 2009, ApJ, 702, 791
Meiring, J. D., et al. 2009, MNRAS, 397, 2037
Monet, D. G., et al. 2003, AJ, 125, 984
Noda, K., et al. 2009, GRB Coordinates Network, 9951, 1
Oates, S. R., & Vetere, L. 2009, GRB Coordinates Network, 9948, 1
Panaitescu, A., & Mészáros, P. 1999, ApJ, 526, 707
Perna, R., & Loeb, A. 1998, ApJ, 501, 467
Piran, T. 2004, Rev. Mod. Phys., 76, 1143
Pontzen, A., et al. 2009, MNRAS, 1943
Prochaska, J. X. 2006, ApJ, 650, 272
Prochaska, J. X., Castro, S., & Djorgovski, S. G. 2003, ApJS, 148, 317
Prochaska, J. X., Chen, H., & Bloom, J. S. 2006, ApJ, 648, 95
Prochaska, J. X., Dessauges-Zavadsky, M., Ramirez-Ruiz, E., & Chen, H. 2008, ApJ, 685, 344
Prochaska, J. X., et al. 2007, ApJS, 168, 231
Racusin, J. L., et al. 2009, ApJ, 698, 43
Rau, A., Salvato, M., & Greiner, J. 2005, A&A, 444, 425
Rhoads, J. E. 1997, ApJ, 487, L1
Sari, R., Piran, T., & Halpern, J. P. 1999, ApJ, 519, L17
Sari, R., Piran, T., & Narayan, R. 1998, ApJ, 497, L17
Savage, B. D., & Sembach, K. R. 1991, ApJ, 379, 245
Savaglio, S. 2006, New J. Phys., 8, 195
Savaglio, S., & Fall, S. M. 2004, ApJ, 614, 293
Savaglio, S., Fall, S. M., & Fiore, F. 2003, ApJ, 585, 638
Savaglio, S., Glazebrook, K., & LeBorgne, D. 2009, ApJ, 691, 182
Schlegel, D. J., Finkbeiner, D. P., & Davis, M. 1998, ApJ, 500, 525
Shaver, P. A., McGee, R. X., Newton, L. M., Danks, A. C., & Pottasch, S. R. 1983, MNRAS, 204, 53
Skrutskie, M. F., et al. 2006, AJ, 131, 1163
Spitzer, L. 1978 (ed.), Physical Processes in the Interstellar Medium (New York: Wiley)
Starling, R. L. C., et al. 2005, A&A, 442, L21
Svensson, K.M., Levan, A.J., Tanvir, N.R., Fruchter, A.S., & Strolger, L.-G. 2010, MNRAS, 405, 57
Tody, D. 1993, in ASP Conf. Ser. 52, Astronomical Data Analysis Software and Systems II, ed. R. J. Hanisch, R. J. V. Brissenden, & J. Barnes (San Francisco, CA: ASP), 173
Uehara, T., Takahashi, H., & McEnery, J. 2009, GRB Coordinates Network, 9934, 1
Usov, V. V. 1992, Nature, 357, 472
Vetere, L. 2009, GRB Coordinates Network, 9961, 1
Vetere, L., Evans, P. A., & Goad, M. R. 2009, GRB Coordinates Network, 9936, 1
Vreeswijk, P. M., et al. 2006, A&A, 447, 145
Vreeswijk, P. M., et al. 2007, A&A, 468, 83
Watson, D., et al. 2007, ApJ, 660, L101
Waxman, E., & Draine, B. T. 2000, ApJ, 537, 796
Wijers, R. A. M. J., et al. 1999, ApJ, 523, L33
Wilms, J., Allen, A., & McCray, R. 2000, ApJ, 542, 914